ADVANCED FUNCTIONAL MATERIALS
www.afm-journal.de

Multifunction Hydrophobic Ligand Engineered Cd(S, Se)/ZnS Quantum Dots for Stabilizing Highly Efficient Carbon-Based Perovskite Solar Cells

*Mengmeng Yuan, Xiaoyu Gu, Yizhao Wang, Kausar Ali Khawaja, Jonathan Cappola, Christopher Picart, Lin Li, and Feng Yan**

The long-term operational stability of perovskite solar cells (PSCs) remains a key challenge impeding their commercialization, particularly due to ambient environments (e.g., moisture, oxygen, heat)-induced degradation. Carbon electrode-based PSCs have emerged as cost-effective and relatively stable alternatives to metal electrode-based devices due to carbon materials' hydrophobic behavior, yet they still lag in both long-term durability and power conversion efficiency (PCE). In this work, an ultrathin hydrophobic ligand-modified core–shell Cd(S,Se)/ZnS quantum dots (QDs) capping layer is introduced as a multifunctional interfacial modifier for carbon-electrode-based PSCs. This oleic acid ligand-modified QDs capping layer exhibits inherent hydrophobicity, effectively serving as a moisture barrier to retard perovskite degradation under ambient conditions. Furthermore, the strong interfacial bonding between the QDs and perovskite halide surfaces leads to efficient trap state passivation, reducing trap density and creating a more uniform electrical contact. The modified QDs/perovskite interface also features an elevated conduction band edge, promoting improved charge extraction. As a result, devices incorporating this quantum dot capping layer retain 98% of their initial PCE after 450 h of ambient aging and achieve a champion efficiency of 20.74%. This strategy highlights the potential of hydrophobic ligand-modified chalcogenide QDs as surface modifiers to enhance both the stability and performance of carbon-based PSCs, offering a promising route toward scalable fabrication of durable perovskite solar modules.

1. Introduction

Halide perovskite solar cells (PSCs) have garnered significant interest for photovoltaic applications due to their exceptional optoelectronic properties, such as a high absorption coefficient with a power conversion efficiency (PCE) of 27%,[1,2] long carrier diffusion length,[3,4] and tunable bandgap.[5,6] Given the advantages of PSCs over traditional thin-film technologies such as CdTe and Cu(In, Ga)Se_2, the rapid upscaling of large-area perovskite solar module (PSM) manufacturing is now underway. Particularly, to reduce the manufacturing cost of the PSMs, cost-effective carbon-based perovskite solar cells (C-PSCs) have become popular by filling the efficiency gap of the noble metal-based PSCs. However, PSCs technology still suffers from inherent device performance limitations, including sensitivity to moisture and oxygen,[7,8] as well as surface defects that act as nonradiative recombination centers, reducing efficiency and long-term stability.[9,10]

To address these issues, various strategies have been developed, such as composition engineering,[9,11] additive incorporation,[12,13] and a nonstoichiometric approach.[9] Among these, using quantum dots (QDs) as post-treatment agents has emerged as a promising approach.[14–18] For example, carbon quantum dots can improve light absorption and have been used for perovskite to improve the device performance; however, they still need to prevent the moisture attack for the perovskite film.[19,20] In addition, adding inorganic perovskite $CsPbBrCl_2$ QDs into the precursor solution facilitates the uniform distribution of elemental dopants within $MAPbI_3$ films and promotes effective ligand attachment, which reduces band-tail states and trap densities while extending carrier lifetimes.[21] Adaptating $CsPbI_3$ quantum dots as an intermediate layer between the perovskite and hole transport layer can also promote the efficiency.[22–24] Doped $CsPb(I, Br)_3$ QDs can play as nucleation centers to promote perovskite grain growth, mitigate nonradiative recombination, and enhance hydrophobicity, thereby improving environmental stability.[17,25] Although forming a 0D (perovskite quantum dot)/3D (perovskite absorber) structure can boost charge transport, refine film morphology, and passivate defects, the inherent soft ionic lattice of perovskite renders it highly susceptible to degradation from water and air.[22–24] Consequently, this approach does not fundamentally resolve the stability issues of perovskite thin-film devices. This makes the

M. Yuan, X. Gu, Y. Wang, K. A. Khawaja, J. Cappola, C. Picart, L. Li, F. Yan
Materials Science and Engineering Program
School for Engineering of Matter, Transport, and Energy
Arizona State University
Tempe, AZ 85287, USA
E-mail: fengyan@asu.edu

The ORCID identification number(s) for the author(s) of this article can be found under https://doi.org/10.1002/adfm.202515519

DOI: 10.1002/adfm.202515519

stable chalcogenide QDs promising for integrating with PSCs become promising. Chalcogenide QDs, such as PbS, CdSe, SnS, ZnSe QDs, act as additives in perovskite solar cells, can boost the PCE and stability by reducing bulk recombination, and improve light harvesting.[26–28]

To date, various approaches have been developed to integrate these QDs into PSCs, such as forming heterostructures, modifying the interface, and embedding within the perovskite active layer.[21,29–32] Particularly, QD-based capping layer between the perovskite and the hole transport layer (HTL) offers a more straightforward and effective way to prevent the lattice mismatch and dispersion challenges between QDs and perovskite matrix.[33–35] The QDs interfacial layer not only impedes moisture ingress but also refines the interfacial alignment, facilitating efficient charge extraction and reducing nonradiative recombination.[33] However, achieving ideal band alignment between the chalcogenide QDs capping layer and the perovskite layer remains a significant challenge for ensuring efficient charge transfer.[36,37]

In this study, we utilize core–shell Cd(S,Se)/ZnS QDs with a fluorescence emission centered at 668 nm to simultaneously enhance the environmental stability and performance of carbon-based perovskite solar cells. The Cd(S,Se) core, encapsulated by a ZnS shell, provides robust optical and electronic passivation. The ZnS shell effectively suppresses nonradiative recombination, while the ultrathin oleic acid surface ligands impart hydrophobicity, as evidenced by increased water contact angles. In addition to its inherent hydrophobicity, which acts as an effective moisture barrier and enhances environmental stability, the Cd(S,Se)/ZnS QDs layer also provides chemical passivation at the perovskite surface and suppresses halide ion migration. This multifunctional hybrid organic–inorganic interface thus serves as a dual-purpose capping layer, offering both physical protection and interfacial defect passivation, collectively contributing to improved operational stability of C-PSCs. We systematically investigate the impact of Cd(S,Se)/ZnS QDs treatment on the optoelectronic properties, surface morphology, and environmental stability of $Cs_{0.1}FA_{0.9}PbI_{2.955}Br_{0.045}$ films. By exploring mechanisms such as surface trap passivation, spectral conversion, and hydrophobic enhancement, this research provides new insights into the use of chalcogenide QD interfacial engineering to improve both the efficiency and durability of perovskite solar technologies.

2. Results and Discussion

As illustrated in **Figure 1a**, pristine perovskite films were initially fabricated via a spin-coating process and subsequently annealed at 110 °C for 30 min in ambient air. Following this, a dispersion of QDs in toluene was spin-coated onto the films at 3000 rpm for 30 s. The QDs, with a diameter of ≈6 nm and a 1.5–1.8 nm oleic acid ligand monolayer, were uniformly deposited onto the perovskite surface.[38–40] The resulting films were then annealed again at 120 °C for 2 min to remove residual toluene and promote uniform QD coverage. The PL spectrum of the QDs, featuring a prominent peak at ≈668 nm, is presented in Figure 1b. Additionally, the bright red emission observed under UV illumination (inset) further confirms their strong luminescence. The Cd(S,Se)/ZnS core–shell architecture, combined with surface-bound ultrathin oleic acid ligands, ensures excellent colloidal stability in toluene, enabling efficient and uniform deposition via spin coating. SEM images (Figure 1c) provide a comparative analysis of perovskite films with (w QDs) and without QDs (w/o QDs) coating. After applying the QDs layer, the films display denser coverage with fewer grain-boundary gaps. This observation indicates that QDs effectively fill the voids at grain boundaries, resulting in smoother, more compact surfaces. It is expected that the hydrophobic oleic acid ligand in the QDs could significantly repel the moisture attack on the pristine perovskite, as shown in Figure 1a. In particular, the QDs can also passivate grain boundaries, providing an additional barrier against moisture ingress through these vulnerable pathways. Figure 1d compares the absorption spectra of QD films, pristine perovskite films, and QD-coated perovskite films. The QDs primarily exhibit absorption in the visible range between 600 and 700 nm (Figure S1, Supporting Information), as further confirmed by their PL peak at 668 nm. In contrast, the perovskite films demonstrate strong absorption ≈800 nm. The combined film demonstrates overlapping absorption characteristics from both materials in the visible spectrum. As shown in Figure 1e, a magnified view of the 760–820 nm region reveals that QD incorporation does not significantly alter the perovskite absorption edge but introduces complementary absorption in the visible region. From the Tauc plot (Figure 1f), the bandgap of the perovskite film is determined to be ≈1.54 eV, while that of the quantum dots is ≈1.81 eV, consistent with the PL spectra. The strong luminescence and relatively larger bandgap of the QDs may enable complementary visible-light absorption and efficient spectral conversion, potentially enhancing the device's overall photon harvesting efficiency, which will be discussed later.

The XRD patterns of perovskite films with and without QD treatment are shown in **Figure 2a**. Both exhibit characteristic diffraction peaks at $2\theta = 14.0°$ (001) and 28.2° (002), corresponding to the typical 3D perovskite crystal structure. An enlarged view of these two main peaks (Figure 2b) highlights a slight increase in peak intensity for the QDs-treated film, suggesting improved crystallinity or enhanced preferential orientation. Enhanced diffraction intensity typically correlates with more ordered lattice stacking and fewer grain-boundary defects, aligning with improved device performance, as discussed later. No additional diffraction peaks emerge, suggesting that the QD coating does not introduce secondary phases or impurities. Further structural insights are obtained from GIWAXS measurements at a grazing-incidence angle of 0.1° (Figure 2c). Compared to the control, the QD-coated film shows sharper and more defined diffraction arcs, implying improved crystallographic ordering and orientation near the film surface. Notably, no distinct diffraction features from the QDs are detected, suggesting their incorporation without disrupting the perovskite crystal framework. Similar GIWAXS patterns obtained at incidence angles of 0.5° and 1° are provided in Figure S2 (Supporting Information) and support these observations.

To quantify these observations, azimuthal integration was performed on the GIWAXS data (Figure 2d,e). At 0.1°, the QD-treated perovskite film exhibits an enhanced diffraction peak at $q = 1.984$ Å^{-1}, corresponding to the (200) plane—a favorable orientation for vertical carrier transport.[41] This is consistent with

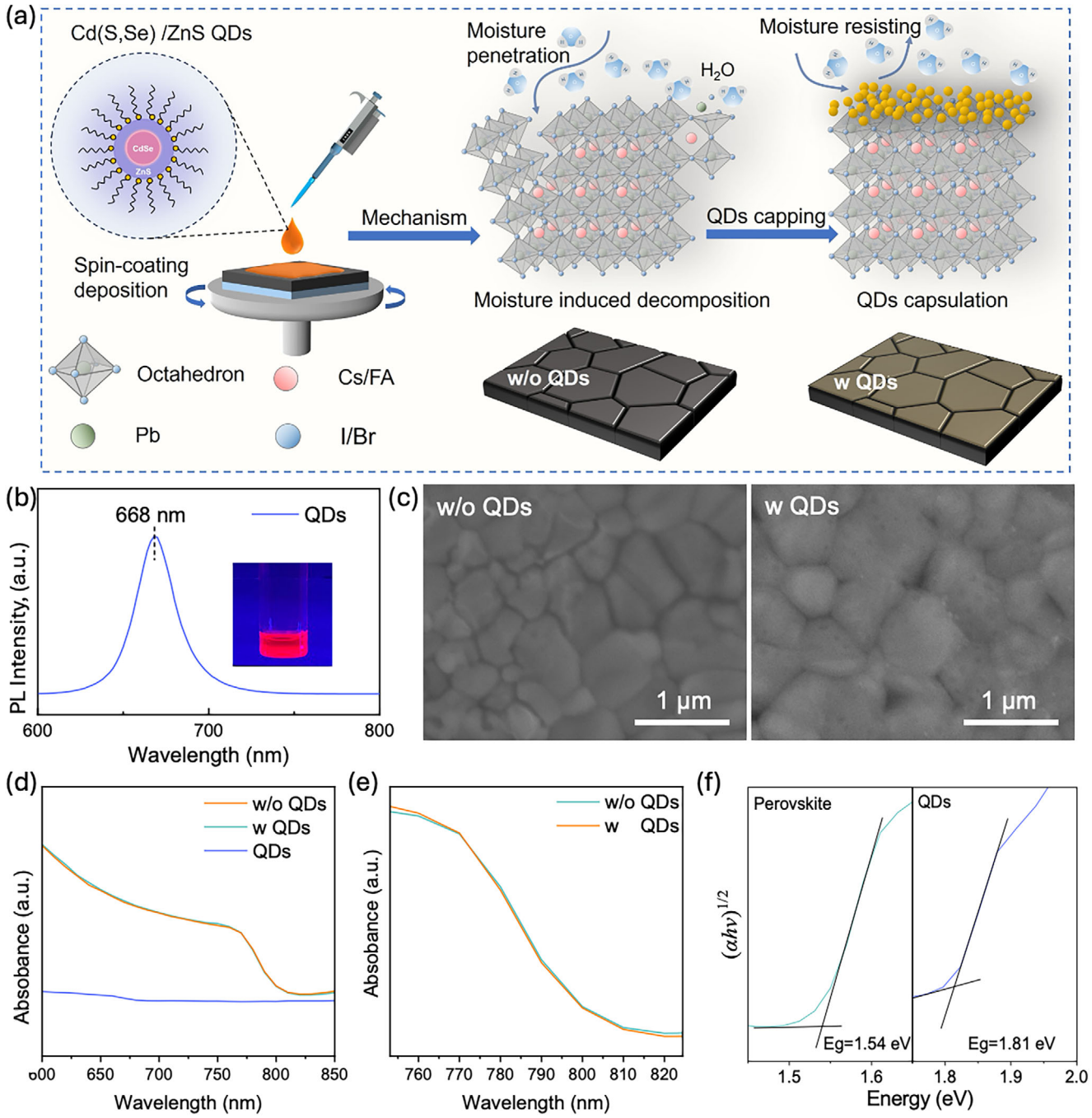

Figure 1. Schematic of Cd(S,Se)/ZnS core–shell QDs coating on Perovskite and associated optical properties. a) Schematic illustration of nucleation and crystallization procedures during the formation of perovskite films and quantum dot surface modification. b) Photoluminescence (PL) image of Cd(S,Se)/ZnS core–shell type quantum dots dispersion in toluene. The inset shows their luminescence under UV light. c) Top-surface Scanning Electron Microscopy (SEM) images of the perovskite films without and with QDs. d) UV–vis optical absorption spectra of QD films, perovskite films with and without QDs. e) Enlarged view of (d). f) Tauc plots of the perovskite and Cd(S,Se)/ZnS QDs.

the corresponding XRD peak near $2\theta = 28.14°$. The d-spacing was calculated using the reciprocal space relation $d = \frac{2\pi}{q}$, and the Bragg angle was determined using Bragg's law $n\lambda = 2dsin\theta$. Moreover, GIWAXS profiles collected at different grazing angles demonstrate that the intensity enhancement is only apparent at small angles. As the grazing angle increases from 0.1° to 1° (Figure 2e; Figure S3, Supporting Information), the intensity difference between the QD-treated and control films diminishes. Since GIWAXS at 0.1° probes only the top ≈10 nm of the film,[42] this depth-dependent behavior provides strong evidence that the

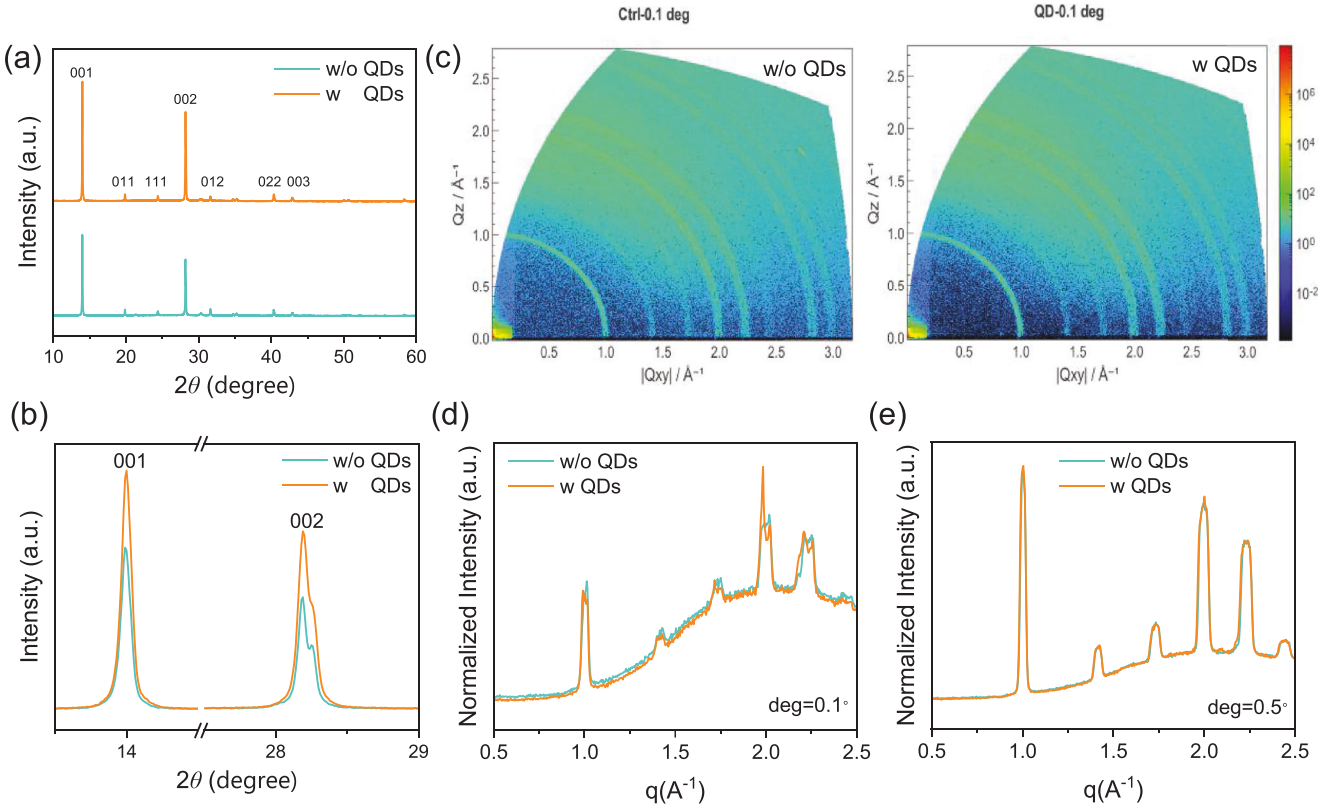

Figure 2. Structural characterization of perovskite thin films without and with QDs spin-coating. a) X-ray diffraction (XRD) patterns. b) Enlarged view highlighting the main diffraction peaks (001 and 002) from panel (a). c) Grazing-incidence wide-angle X-ray scattering (GIWAXS) patterns, measured at an incidence angle of 0.1°. GIWAXS line-cut profiles of control and QD-treated perovskite films, acquired at incidence angles of (d) 0.1° and (e) 0.5°, based on azimuthal integration of the 2D GIWAXS patterns.

QD layer primarily enhances crystallographic ordering near the perovskite surface.

To investigate the distribution of QDs within the perovskite film, elemental depth profiling was performed using GD-OES, as shown in **Figure** 3a,b. The depth profiles of key elements in perovskite films with and without QDs were tracked. Core perovskite elements such as Pb and I remain relatively uniform throughout the film thickness. In contrast, Cd, Zn, and Se (originating from the QDs) are predominantly localized near the film surface and rapidly diminish with depth, indicating that QDs are confined to the uppermost region and do not significantly diffuse into the perovskite bulk. Notably, QD-related signals remain detectable even after chlorobenzene (CB) rinsing (Figure S4, Supporting Information), suggesting their retention during the subsequent spiro-OMeTAD deposition process. Interestingly, the iodide profile in the QD-capped perovskite shows accumulation at the QDs/perovskite interface, whereas the pristine film exhibits surface iodine loss. This implies that the QDs capping layer may mitigate surface iodine depletion, potentially alleviating degradation pathways associated with halide instability.

Further evidence of interfacial chemical interactions is provided by XPS analysis (Figure 3c–e; Figure S5, Supporting Information). Upon QD treatment, the I $3d_{5/2}$ peak shifts from 618.4 to 619.1 eV, the Cd $3d_{5/2}$ peak from 404.9 to 405.2 eV, and the Zn $2p_3/_2$ peak from 1021.8 to 1020.8 eV. The I 3d and Cd 3d peaks toward higher binding energies, along with the downward shift of Zn 2p, collectively suggest electron redistribution at the perovskite/QD interface. Specifically, the coordination of iodide ions (acting as Lewis bases) with Cd^{2+} and Zn^{2+} (strong Lewis acids with low electronegativity) leads to electron withdrawal from I^- to Cd^{2+}—increasing the binding energies of both. In contrast, Zn^{2+} likely forms more covalent or polarizable Zn–I interactions, possibly gaining electron density, which is reflected in its decreased binding energy. These shifts provide strong evidence of interfacial chemical interactions between QD and surface iodide ions, possibly stabilizing them and acting as an Iodine diffusion blocking layer. This interaction may also involve the surface reaction: $Cd^{2+}/Zn^{2+} + 2I^- = (Cd/Zn)I_2$, leading to the formation of a surface CdI_2/ZnI_2-like interface that suppresses iodine diffusion toward the back contact and retards perovskite decomposition driven by high halide chemical potential at the surface. This proposed interaction is schematically illustrated in Figure S6 (Supporting Information), where surface-deposited QDs selectively coordinate with migrating iodide ions, forming a directional iodine-affinity barrier that blocks further halide diffusion and stabilizes the interface. To further clarify whether the surface passivation and interfacial modification effects arise from the QDs themselves or the organic ligands associated with their synthesis, we conducted a control experiment using oleic acid (OA) alone (without the presence of QDs) under the same spin-coating conditions. As shown in Figure S7 (Supporting Information), the

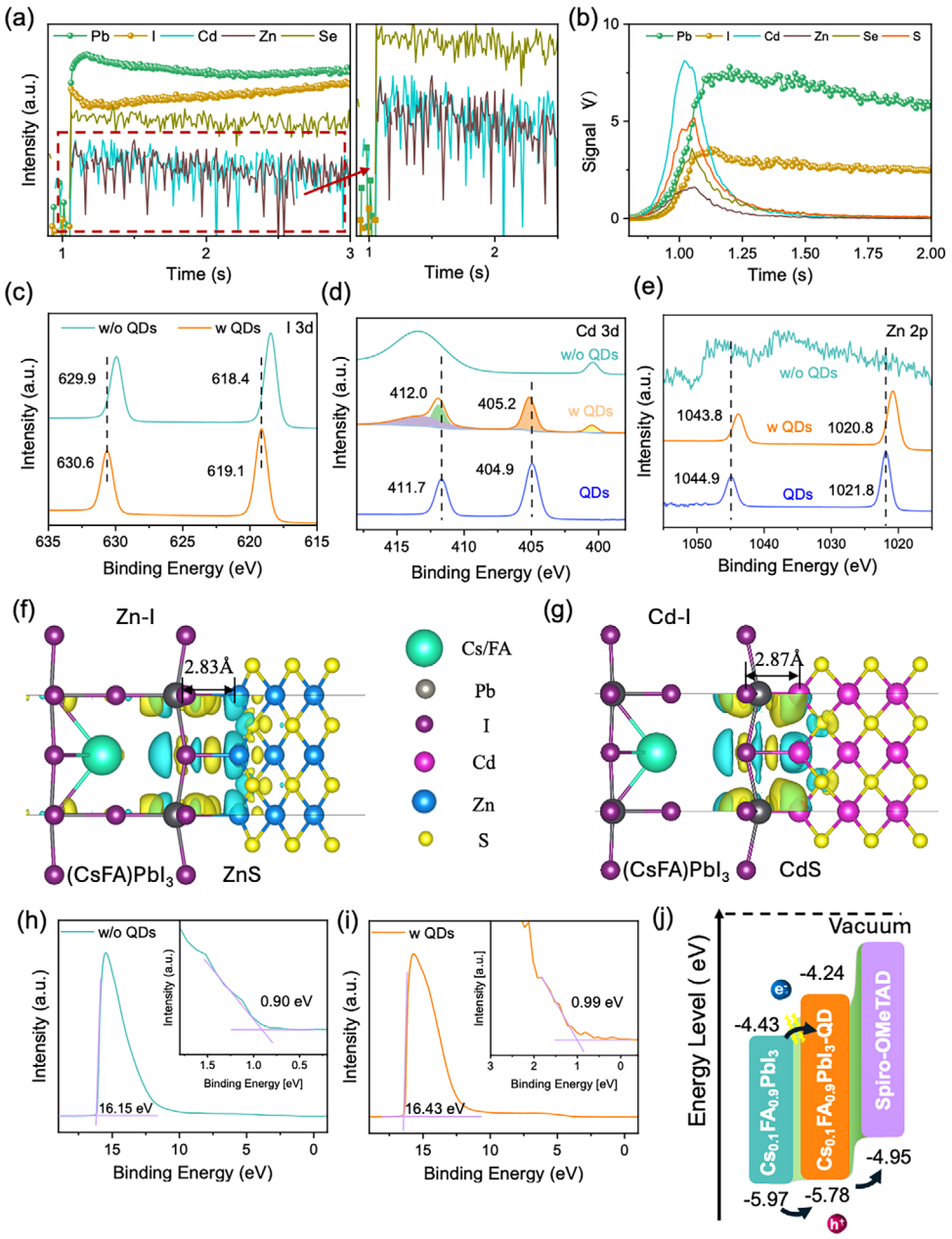

Figure 3. Variations in the chemical properties of perovskite films upon QD capping. a) glow-discharge optical emission spectroscopy (GD-OES) of the pristine perovskite film (left) and its enlarged view (right), b) GD-OES profile of the perovskite film after QD capping. c–e) X-ray photoelectron spectroscopy (XPS) for I 3d (c), Cd 3d (d), and Zn 2p (e) in perovskite films with and without QDs. f,g) density-function-theory (DFT) calculated local bonding structure between perovskite and quantum dot to form Zn—I and Cd—I, respectively. h–j) Ultraviolet photoelectron spectra (UPS): magnified cutoff (E_{cutoff}) energy regions, and valence band region (VBM) onset regions of the perovskite films without and with QDs, respectively. j) Corresponding energy-level diagram comparing the energy levels of perovskite and QDs-capped perovskite.

XPS spectra of Pb 4f, I 3d, Br 3d, and Cs 3d show no significant changes compared to the pristine film, suggesting that oleic acid alone does not contribute to effective defect passivation. To probe the potential interfacial reaction between quantum dots and the perovskite surface, we conducted a model experiment by mixing CdSe with PbI_2 and applying thermal treatment to simulate reaction conditions. FTIR measurements (Figure S8, Supporting Information) did not reveal significant changes, likely because the Cd—I vibrational modes lie in the far-infrared region beyond the detection range of conventional FTIR. In contrast, Raman spectroscopy (Figure S9, Supporting Information) revealed clear spectral differences between pristine CdSe and the CdSe–PbI_2 mixture. New peaks appeared at 65.6 cm^{-1}, which we attribute to the formation of Cd—I bonds. Additionally, a slight shift of the PbI_2 peak from 105.6 to 106.5 cm^{-1} suggests possible vibrational coupling with Cd—I modes. These results support the formation of

Cd—I species, providing indirect evidence for the proposed surface reaction between QDs and perovskite.

To further validate the interface reaction between the perovskite and quantum dots, a DFT-based interface charge density calculation has been performed. As shown in Figure 3f,g, the structurally optimized perovskite/ZnS and perovskite/CdS interfaces, including the charge density difference, have been calculated, which illustrates the charge redistribution from chemical bonding for the Zn—I and Cd—I bonds. The Zn—I shows a lifting of the I atoms from the PbI_2 plane by 0.52Å (Figure 3f), while the Cd—I configuration (Figure 3g) exhibits a lifting of the Pb atom by 0.67Å from the PbI_2 plane. When (Cd/Zn) is bonded to I, a consistent charge transfer of ≈−0.5eV to the I atoms in the PbI_2 plane. Examining the isocontours of charge density differences in the (Cd/Zn)—I configurations exhibits a significant charge accumulation around the nearest-neighbor Pb atoms, which is indicative of stronger bonding. The detailed calculation results are listed in Figure S10 and Table S8 (Supporting Information). This indicates that the (Cd/Zn)S/perovskite interfaces are thermodynamically stable.

UPS further confirms energy-level modulation after QD treatment. As shown in Figure 3f,g, the secondary electron cutoff (E_{cutoff}) shifts from 16.15 eV (pristine) to 16.43 eV (QD-treated), while the valence band onset (E_{onset}) moves from 0.90 to 0.99 eV, indicating an increase in the work function. Based on this UPS data and the bandgap information from Figure 1f, the energy level diagram (Figure 3h) was constructed. After QD capping, the conduction band maximum (CBM) shifts from ≈−4.43 to −4.24 eV, and the valence band minimum (VBM) shifts from −5.97 to −5.78 eV, with respect to the vacuum level. These changes reflect an upward shift in the Fermi level (E_F) toward the CBM, which can suppress surface nonradiative recombination by facilitating hole extraction. The relatively wide bandgap of QDs also contributes to forming an interfacial energy gradient, which not only passivates surface defects but also facilitates or blocks specific carrier processes. These interfacial modifications contribute to enhanced charge separation and carrier transport, ultimately improving device performance and operational stability.

To further determine the energy level shift observed in UPS and its influence on device performance, we performed SCAPS-1D simulations using experimentally determined parameters, including the UPS-extracted work function and bandgap values (Figure 1f; Figure S11, and Table S1, Supporting Information). As shown in Figure S12 (Supporting Information), the QD-modified device exhibits a more favorable alignment between the perovskite VBM and the Spiro-OMeTAD HOMO level, reducing the interfacial energy barrier for hole extraction. The simulated band diagrams (Figure S12, Supporting Information) reveal that the control device features a larger VBM–HOMO offset, forming a potential barrier that may hinder hole transport. In contrast, the QD-treated device shows smoother band bending and a reduced offset, consistent with the increased work function measured by UPS. This improved alignment is further supported by TRPL (**Figure** 4c) and TPC (Figure S13, Supporting Information) results, which show faster carrier extraction and reduced trap-mediated recombination at the interface. To quantitatively assess the impact of this interfacial tuning, *J–V* simulations were performed (Figure S14, Supporting Information). The QD-modified device shows an increased open-circuit voltage (V_{oc}), closely matching experimental data and indicating suppressed interfacial recombination. The simulated J_{sc}, FF, and PCE are also in good agreement with measured values (Table S2, Supporting Information), confirming that the energy level alignment observed in UPS directly translates into improved device performance, as supported by both optical measurements and numerical modeling.

To investigate photonic behavior via utilizing the QDs capping layer on the pristine perovskite layer, PL emissions, TRPL, and PL mapping from perovskite films with and without QDs are recorded under identical excitation conditions, as shown in Figure 4. Figure 4a presents that the QD-capped perovskite film shows a significantly stronger main PL peak (780 nm) with a narrower full width at half maximum (FWHM), indicating suppressed surface defect states and a reduced radiative recombination rate. A shoulder near 668 nm, attributed to the QDs' emission, slightly overlaps with the perovskite peak and is visible on the high-energy side (Figure S15, Supporting Information).

To gain further insight into charge recombination dynamics and hole extraction efficiency, TRPL measurements were performed on two sets of structures: glass/perovskite versus glass/perovskite/QDs (Figure 4b), and glass/perovskite/Spiro versus glass/perovskite/QDs/Spiro (Figure 4c). The average PL lifetime (τ_{ave}) was calculated using $\tau_{ave} = \frac{A_1\tau_1^2+A_2\tau_2^2}{A_1\tau_1+A_2\tau_{\tau 2}}$ and detailed fitting parameters are listed in Tables S3 and S4 (Supporting Information). In the absence of a transport layer, τ_{ave} increases from 290.9 (pristine film) to 670.7 ns after QD treatment, clearly indicating effective defect passivation and suppression of nonradiative pathways within the perovskite layer (Figure 4b). In contrast, when Spiro-OMeTAD is introduced, the PL lifetime shortens due to carrier extraction: τ_{ave} drops from 36.4 (without QDs) to 19.8 ns (with QDs), as shown in Figure 4c. This faster decay does not imply increased recombination but rather reflects enhanced hole extraction facilitated by improved energy level alignment at the perovskite/Spiro interface induced by the QD interlayer.

Spatially resolved PL peak mapping (Figure 4d–f) and intensity mapping (Figure 4g–i) further highlight the role of QDs in improving film homogeneity. Compared to the pristine film (Figure 4d), the QD-coated film (Figure 4e) exhibits more uniform peak position distribution, indicating a more homogeneous strain and compositional environment. To evaluate whether the beneficial effects of QDs persist through the subsequent Spiro-OMeTAD deposition step, which involves exposure to chlorobenzene (CB), we conducted a CB washing test. The QDs-modified film maintains its uniform PL profile (Figure 4e) even after CB washing, confirming robust attachment of QDs to the perovskite surface. PL intensity maps (Figure 4g–i) further highlight differences in emission uniformity, underscoring the effectiveness of the QDs surface passivation strategy. The pristine film (Figure 4g) contains regions of notably weaker PL, likely corresponding to defect-rich clusters or grain boundaries. In contrast, the QD-capped film (Figure 4h) exhibits stronger and more uniform PL intensity, implying reduced nonradiative recombination. After CB washing, strong PL emission is still preserved (Figure 4i), indicating that the beneficial passivation effect of QDs remains intact through subsequent processing.

To complement the photophysical insights from TRPL and further assess the effect of QDs on charge transport dynamics, we

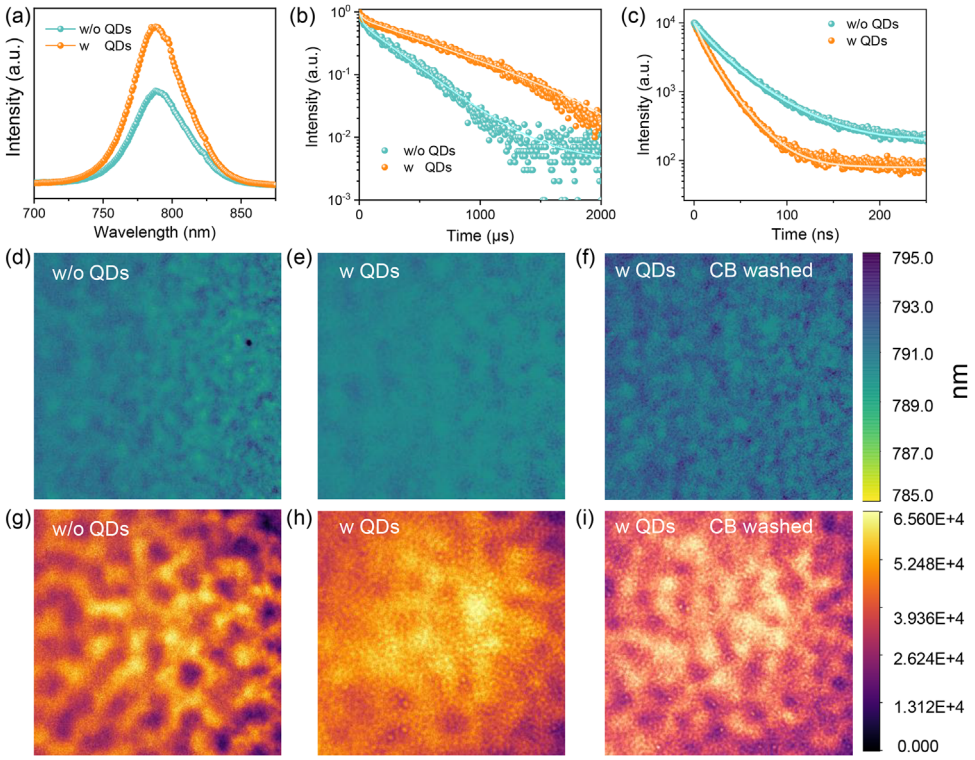

Figure 4. Effects of QD coating on carrier recombination dynamics and optical uniformity of perovskite films. a) PL signals of perovskite films with and without QDs. b) Time-resolved photoluminescence (TRPL) spectra of samples with a structure of glass/perovskite and glass/perovskite/QDs. c) TRPL spectra of samples with a structure of glass/perovskite/Spiro and glass/perovskite/QDs/Spiro. d–f) PL peak position mapping of perovskite films: without QDs (d), with QDs (e), and with QDs followed by CB washing (f). g–i) PL intensity mapping of the corresponding films in (d–f), respectively.

conducted transient photocurrent (TPC) measurements at the device level (Figure S13 and Table S5, Supporting Information). The photocurrent decay was fitted using a bi-exponential model: $I(t) = A_1 e^{\frac{-t}{\tau_1}} + A_2 e^{\frac{-t}{\tau_2}}$, where τ_1 represents fast free-carrier extraction and τ_2 corresponds to slower trap-assisted recombination. Compared to the control, the QD-modified device exhibits a faster decay profile, with the average carrier lifetime reduced from 3.00 to 1.72 μs. This shortened lifetime reflects more efficient charge extraction and reduced trap-assisted reemission. These results confirm that the QD interlayer not only passivates shallow traps but also facilitates interfacial transport, in agreement with the improved energy-level alignment from UPS and faster PL decay observed in TRPL measurements.

The device's performance measured via *J–V* curves reveals a modest improvement in power conversion efficiency for the QD-modified devices (**Figure 5a**). Specifically, the reverse-scan PCE increases from 19.6% to 20.74% after introducing the QDs capping layer, which can be attributed to suppressed nonradiative recombination and improved interfacial energy level alignment. The corresponding photovoltaic parameters for devices based on pristine and QD-coated perovskite films are summarized in **Table 1**. Interestingly, QD-coated devices exhibit slightly enhanced hysteresis compared to control devices. This behavior may be attributed to interfacial electric field modulation and the intrinsic dipole moments of the CdSeS/ZnS QDs, originating from their core/shell structure and polar ligands. Such effects may increase charge accumulation at the interface, which could amplify hysteresis behavior under certain scan directions. Similar observations have been reported in the literature where interfacial layers, although improving performance, may affect transient charge dynamics.[43–44] To better evaluate performance reproducibility, statistical device performance for the PCE, open circuit voltage (*Voc*), short circuit current (*Jsc*), and fill factor (FF) from twenty devices fabricated within the same batch are compared (Figure S16, Supporting Information). QD-treated devices exhibit not only a higher champion efficiency but also significantly reduced statistical deviation, indicating enhanced uniformity and improved batch-to-batch consistency. As shown in Figure 5b, the QD-coated devices exhibit enhanced EQE in the 300–500 nm range, primarily attributed to effective surface passivation and enhanced carrier extraction by the QD layer. This reduces non-radiative recombination near the illuminated side of the perovskite layer, where high-energy photons are predominantly absorbed. The improved carrier collection efficiency is supported by reduced trap density, as confirmed by SCLC, PL, and TRPL measurements and DFT calculations. Additionally, the QD layer improves energy-level alignment at the perovskite/HTL interface, facilitating more efficient hole extraction and further contributing to the enhanced EQE response at short wavelengths. Nyquist plots extracted from EIS provide further insights into charge transport and recombination behavior (Figure 5c). QD-modified devices exhibit a smaller high-frequency semicircle, indicating lower charge transfer re-

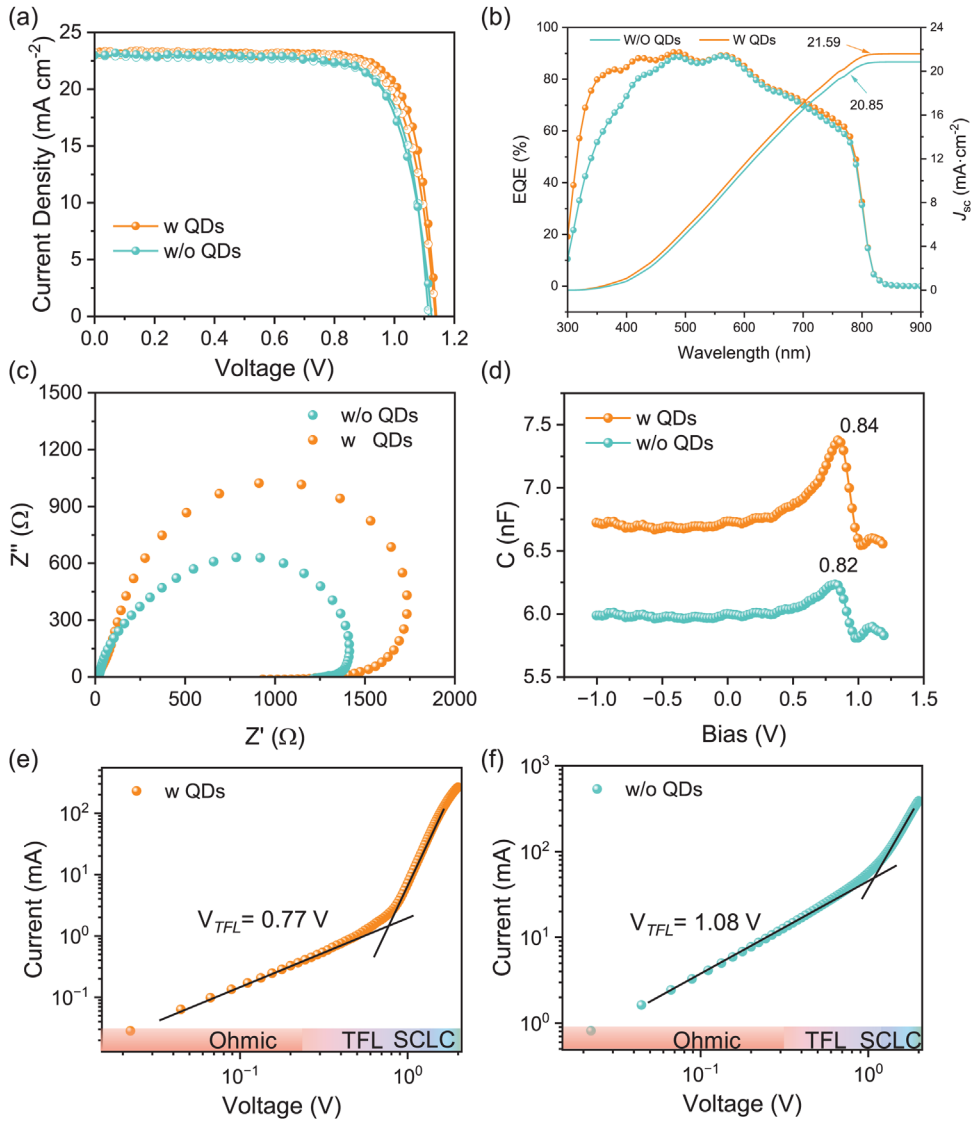

Figure 5. Device performance comparison for perovskite solar cells with and without QDs. a) Current density–voltage (*J*–*V*) curves of devices under forward (Fr) and reverse (Re) scan directions. b) External quantum efficiency (EQE) spectra. c) Electrochemical impedance spectroscopy (EIS) Nyquist plots of perovskite films. d) Capacitance–voltage (*C*–*V*) characteristics of perovskite films. e,f) space charge limited current (SCLC) analysis for w and w/o QDs, respectively.

sistance and improved interfacial carrier extraction. Meanwhile, the larger low-frequency arc suggests increased recombination resistance or enhanced chemical capacitance, implying reduced recombination and prolonged carrier lifetime in the QD-treated films. Additionally, CV (Figure 5d) reveals a slight increase in interfacial capacitance (from 0.82 to 0.84 nF), further supporting the conclusion that QDs enhance the interfacial energy barrier and promote more efficient charge separation and collection. To evaluate the effect of QD coating on perovskite surface defects, defect state densities (N_t) were measured via the SCLC method.

Table 1. Champion device performance for the QD capping perovskite.

Condition	Scan direction	V_{OC} (V)	J_{SC} (mA cm^{-2})	FF (%)	PCE (%)	R_S (Ω·cm^2)	R_{SH} (Ω·cm^2)
Control	Forward	1.124	22.97	75.12	19.40	2.75	4993.99
	Reverse	1.114	22.97	76.57	19.60	3.10	7141.94
QD	Forward	1.137	23.22	76.40	20.16	3.17	4360.34
	Reverse	1.140	23.11	78.72	20.74	0.62	6076.94

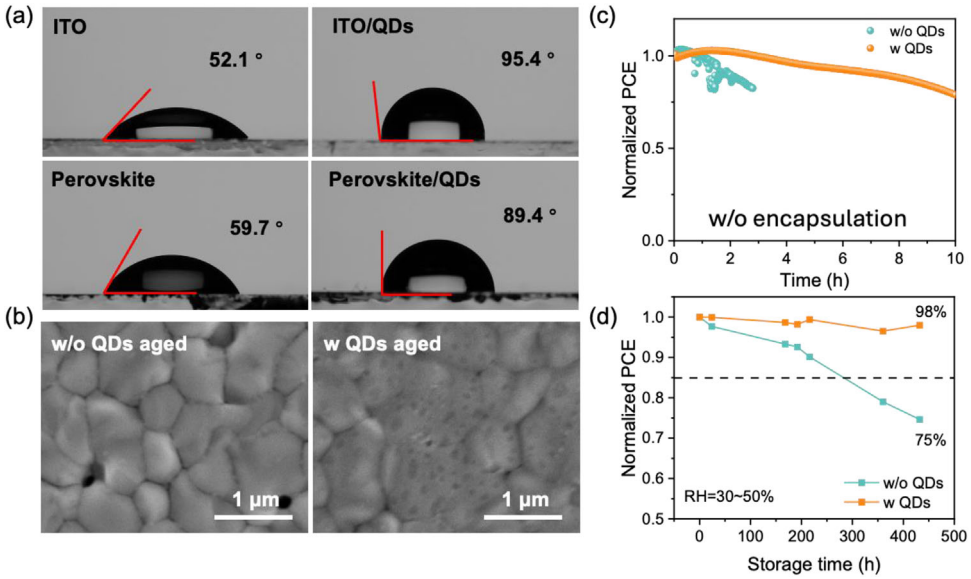

Figure 6. Environmental and operational stability of perovskite films and devices before and after QD spin-coating. a) Water contact angle measurements of ITO glass, QDs-coated glass, perovskite films without QDs, and QDs-coated perovskite films. b) Top-view SEM images of aged perovskite films with and without QDs after 70 h of exposure (relative humidity ≈15–40%). c) Maximum power point (MPPT) tracking performance of devices under continuous operation. d) Long-term storage stability comparison of perovskite devices with and without QDs under ambient conditions (RH = 30–50%).

Dark *I–V* curves of hole-only devices (FTO/PTAA/perovskite/Spiro-OMeTAD/Carbon) are shown in Figure 5e,f. *N*t is determined by the defect filling limit voltage (the onset voltage of the defect filling region) and can be calculated using $N_t = \frac{2V_{TFL}\epsilon_r\epsilon_0}{qd^2}$, where V_{TFL} is the defect filling limit voltage, d is the thickness of the perovskite film, ϵ (with ϵ = 30) is the relative dielectric constant of $Cs_{0.1}FA_{0.9}PbI_{2.955}Br_{0.045}$, and ϵ_0 is the vacuum permittivity. As shown in Figure 5e,f and Table S6 (Supporting Information), V_{TFL} decreases from 1.08 (pristine) to 0.77 V (QD-capped), and the corresponding *N*t drops from 2.67×10^{17} to 1.92×10^{17}, confirming that QD surface treatment effectively reduces defect density from the perovskite film surface.

Water contact angle measurements reveal that the QDs capping layer could significantly increase the surface hydrophobicity, with water contact angle rising from 50–60° to 89–95° on both bare ITO substrate and the perovskite film, as shown in **Figure** 6a. This hydrophobic behavior is primarily attributed to the low surface energy of the long-chain oleic acid ligands and the ZnS shell surrounding the QDs, which effectively repel moisture. The hydrophobicity of the QD layer enhances water resistance, thereby contributing to improved morphological stability of the perovskite film. As shown in Figure S17 (Supporting Information), this effect persists even after CB washing, which further confirms that QDs won't be washed off after the fabrication of the hole transport layer. To decouple the contribution of the OA ligand from that of the quantum dots, a control experiment was performed by spin-coating OA alone onto the perovskite surface. OA is a viscous liquid (viscosity ≈ 25 mPa·s, Table S7, Supporting Information), which poses challenges for forming uniform films via spin coating. As shown in Figure S18 (Supporting Information), OA tends to phase-separate on the perovskite surface, forming nonuniform, liquid-like domains that gradually segregate over time. Contact angle measurements (Figure S19, Supporting Information) reveal that OA-coated perovskite films exhibit a *lower* water contact angle (53.2°) than the pristine film (66.5°), indicating that OA alone does not enhance surface hydrophobicity—likely due to its incomplete coverage and weak binding with the perovskite surface. To evaluate the protective function of the QD layer, an ambient environment storage test has been performed for 70 h under relative humidity (RH) of ≈15–40%. As shown in Figure 6b, the pristine perovskite film exhibits enlarged voids, degraded grain boundaries, and partial crystal collapse. In contrast, the QDs-capped film maintains a compact and uniform morphology, suggesting that the QD layer serves as an effective barrier against moisture and oxygen ingress. While the aged QD-coated film shows slightly blurred surface contrast compared to the fresh film (Figure 1c), this is likely due to the presence of the QD overlayer and residual ligands. Nevertheless, the grain structure remains well preserved, further supporting the protective function of the QD interfacial layer. To further assess device-level operational stability, perovskite solar cells were operated under continuous illumination at their maximum power point, with efficiency recorded every 2 s. As shown in Figure 6c, QD-modified devices retain 80% of their initial efficiency after 10 h, whereas control devices exhibit a sharper decline, maintaining only 82% after just 3 h. This improved stability is attributed to suppressed ion migration and interfacial degradation, consistent with our earlier TRPL, UPS, and TPC analyses. Long-term ambient storage tests further confirm the stabilizing effect of QDs (Figure 6d). After 500 h under RH ≈30–50%, QD-treated devices retain 98% of their initial efficiency, compared to only 75% for untreated ones. The corresponding initial PCE values for both device types are provided in Figure S20 (Supporting Information). To further

evaluate humidity resistance under more stringent conditions, we performed an additional accelerated stability test at RH = 80% for 10 h (Figure S21, Supporting Information). Under this high humidity, QD-modified devices retained 84% of their initial efficiency, while control devices degraded to below 30%. In parallel, surface images of aged perovskite films (Figure S22, Supporting Information) revealed that QD-treated films preserved more uniform and intact morphology, indicating effective protection against moisture-induced degradation. These results collectively demonstrate that QD surface modification provides robust environmental protection and significantly enhances both operational and shelf stability through defect passivation and moisture shielding.

3. Conclusion

A QDs-based surface modification strategy has been shown to enhance both the environmental and operational stability of perovskite films and devices. The QDs capping layer forms a uniform, hydrophobic surface that effectively resists moisture infiltration and environmental degradation. Photophysical characterizations indicate suppressed nonradiative recombination, likely due to reduced surface-related trap states. The modified interface also promotes better energy-level alignment with the hole transport layer, enabling more efficient charge extraction. Additionally, the QDs layer serves as a barrier that inhibits iodide migration from the perovskite bulk toward the electrode, mitigating interfacial degradation. These synergistic effects lead to improved device efficiency and long-term stability, highlighting the potential of 0D (CdSeS/ZnS QDs)/3D (perovskite) interfacial engineering in advancing high-performance perovskite solar cells.

4. Experimental Section

Materials: All chemicals used in this study were obtained from commercial suppliers. The sources and purities of the chemicals were as follows: PbI_2 (>99%, TCI, Japan), CsI (99.999%, Acros), formamidinium iodide (FAI, 99.8%, GreatCell Solar Materials, Australia), methylammonium chloride (MACl, 99.8%, GreatCell Solar Materials, Australia), CsBr (99.9%, Sigma–Aldrich), SnO_2 colloidal dispersion (15 wt.% in H2O, Alfa Aesar, UK), Spiro-OMeTAD (99.7%, Lumtec Co., Taiwan), isopropanol (IPA, 99.8%, Sinopharm Chemical Reagent Co., Ltd, China), 4-tert-butylpyridine (TBP, 96%), Bis(trifluoromethane)sulfonamide lithium salt (Li-TFSI, >98%, Sigma–Aldrich), FK209 Co(III) TFSI (95%, Greatcell solar), Cd(S,Se)/ZnS alloyed quantum dots (1mg/mL in toluene, Sigma–Aldrich), and solvents acetonitrile (99.9%), dimethylformamide (DMF, 99.8%), dimethylsulfoxide (DMSO, 99.9%), α, α, α-Trifluorotoluene (≥99%) and chlorobenzene (CB, 99.8%). The Cd(S,Se)/ZnS quantum dots (Sigma–Aldrich, Product No. 753807 with Lot# [MKBT3770V) used in this work were dispersed in toluene at a concentration of 1 mg mL^{-1} and passivated with oleic acid ligands. As shown in Figure S23 (Supporting Information), the photoluminescence quantum yield (PLQY) of the QD solution was calculated using the following equation:

$$PLQY = \frac{\int \text{Number of emitted photon}}{\int \text{Number of absorbed photon}} = \frac{I_{PL}}{I_{excitation} \times (1 - T\%)} \quad (1)$$

where I_{PL} is the integrated photoluminescence intensity, and T% is the transmittance of the QDs solution at the excitation wavelength. In our experiment, excitation was performed at 350 nm with a 2 nm slit width, and the emission spectrum was collected from 600 to 750 nm with a 0.5 nm resolution. The reference excitation intensity was 3 25 000 counts. Based on the measured PL and transmittance spectra, the calculated PLQY was ≈63.58%, which was consistent with previously reported values for similar core/shell structures, confirming the good optical quality and passivation of the CdSeS/ZnS QDs used in this study.[45]

Device Fabrication: ITO-coated glass substrates were initially wiped with a lint-free cloth and isopropanol, followed by sequential ultrasonic cleaning in detergent, ethanol, and isopropanol. The substrates were then dried using a stream of dry air. Subsequently, the electron transport (hole-blocking) layer of SnO_2 (Alfa Aesar, diluted to 2.67%) was deposited onto the glass/ITO substrates via spin-coating in ambient air with a relative humidity of ≈12% after a 15-min UV-ozone treatment. The spin-coating process was carried out at 3000 rpm for 30 s with an acceleration rate of 3000 rpm s^{-1}. And then the SnO_2 wet film was annealed at 170 °C for 30 min. The perovskite film was fabricated by a one-step vacuum-assisted approach without using an anti-solvent. 1.2M $Cs_{0.1}FA_{0.9}PbI_{2.955}Br_{0.045}$ precursor solution was spin-coated onto SnO_2 at 1000rpm for 10 s and 4000 rpm for 30 s. 30 uL perovskite precursor was spin-coated at 3000rpm 15s^{-1} (1500rpm s^{-1} accelerate) in N_2 glovebox and transferred into ambient air to vacuum degassed for 55s and then annealed at 120 °C for 30 min in RH% 30%-40%. For QD treatment, right after perovskite film deposition, Cd(S,Se)/ZnS QDs were dynamically spin-coated at 3000rpm 30s^{-1} (3000rpm s^{-1} accelerate) and then annealed at 120 °C for 2 min. HTL solution of 72.3 mg 2,2',7,7'-Tetrakis [N, N-di(4-methoxyphenyl)amino]-9,9'-spirobifluorene (Spiro-OMeTAD), 28.8 µL of 4-tert-butylpyridine, and 17.5 µL of 520 mg mL^{-1} Lithium bis(trifluoromethanesulfonyl)imide acetonitrile solution dissolved in 1 mL chlorobenzene was dynamically spin-coated on a perovskite/SnO_2/ITO substrate at 3000 rpm for 30 s. The anode, consisting of a carbon electrode, was prepared using the doctor blade method. Specifically, commercial graphite paste was doctor-bladed into a groove with a precisely controlled depth of ≈40 µm to form a uniform carbon layer (Figure S24, Supporting Information). Immediately following blade coating, the wet carbon film was immersed in ethanol for 20–30 min to effectively remove residual solvents and impurities. Subsequently, the film was dried by blowing with compressed air for ≈5 min and then stored in a dry-air glovebox until further use. Finally, the prepared carbon electrode was attached to the hole transport layer film through hot pressing at 80 °C and 110 psi for 60 s. The silver cathode was annealed at 85 °C for 1 min.

Characterizations: Photo *J–V* were measured using a solar simulator (Newport, Oriel Class AAA 94063A, 1000-Watt Xenon light source) with a Keithley 2420 source meter under simulated AM1.5G (100 mW cm^{-2}, calibrated with a standard Si solar cell) solar irradiation. The active area was defined by a 0.05 cm^2 aperture mask (Figure S25, Supporting Information), and the current–voltage scan rate was 100 mV s^{-1}. The EQE was obtained using an EnliTech QE measurement system. The PL and TRPL were acquired using an Edinburgh Instruments FS5 spectrofluorometer. A Paios was used to collect both the C–V measurements and the EIS characteristics. The SEM images were obtained using an SEM/focused ion beam from Auriga (Zeiss) at an acceleration voltage of 5 kV. The XRD measurements were recorded by a Rigaku SmartLab high-resolution X-ray diffractometer. The GIWAXS measurements were obtained from a Xenocs Xeuss (GI-)SAXS/WAXS/USAXS instrument with a GeniX3D Cu High Flux Very Long (HFVL) focus source as X-ray source and an Eiger2R1M Dectris hybrid pixel silicon sensor as the detector. GD-OES were measured using Horiba GD-Profiler 2 Glow Discharge Optical Emission Spectrometer. Ultraviolet photo-electron spectroscopy (UPS) was conducted using a Thermo Fisher Scientific Analytical spectrometer (ESCALAB 250Xi) and mono-chromatized He–Iα radiation at 21.2 eV. X-ray photoelectron spectroscopy (XPS) analysis was performed with a Thermo Fisher Scientific Analytical spectrometer (ESCALAB 250Xi), and all XPS spectra were adjusted to compensate for sample charging, using inorganic carbon at 284.80 eV as a reference.

Computational Calculation: *Ab-initio* calculations were carried out with VASP[46,47] using the projector-augmented wave method[48] and adopting the Perdew-Burke-Ernzerhof generalized gradient approximation for the exchange-correlation functional.[49] A plane-wave basis set cut-off energy

of 400 eV was used. The Brillouin zone sampled by a 5 × 5 × 1 Γ-centered *k*-point mesh in all supercells with a Gaussian smearing width of 0.1 eV. A tolerance of 1e-6 eV was set for electronic convergence, and a force convergence tolerance of 1e-2 eV $Å^{-1}$ was set for structural relaxations. The device calculation for the perovskite/quantum dot was performed using the SCAPS (a Solar Cell Capacitance Simulator).[50]

Supporting Information

Supporting Information is available from the Wiley Online Library or from the author.

Acknowledgements

M.Y. and X.G. contributed equally to this work. This work was supported by the National Science Foundation under contract Nos. ECCS-2413632, MOMS-2330728, TI-2329871, and DMR-2330738, and CMMI-2226918, and DMREF-2323766. This material is also based upon work supported by the U.S. Department of Energy's Office of Energy Efficiency and Renewable Energy (EERE) under the Solar Energy Technologies Office Award No. DE-EE0009833.

Conflict of Interest

The authors declare no conflict of interest.

Data Availability Statement

The data that support the findings of this study are available from the corresponding author upon reasonable request.

Keywords

carbon electrode, Cd(S,Se)/ZnS quantum dot, hydrophobic ligand, perovskites solar cells, stability

Received: June 18, 2025
Revised: July 31, 2025
Published online:

[1] A. Kojima, K. Teshima, Y. Shirai, T. Miyasaka, *J. Am. Chem. Soc.* **2009**, *131*, 6050.
[2] National Renewable Energy Laboratory, Best Research-Cell Efficiency Chart, https://www.nrel.gov/pv/cell-efficiency.html.
[3] H.-S. Kim, C.-R. Lee, J.-H. Im, K.-B. Lee, T. Moehl, A. Marchioro, S.-J. Moon, R. Humphry-Baker, J.-H. Yum, J. E. Moser, M. Grätzel, N.-G. Park, *Sci. Rep.* **2012**, *2*, 591.
[4] S. De Wolf, J. Holovsky, S.-J. Moon, P. Löper, B. Niesen, M. Ledinsky, F.-J. Haug, J.-H. Yum, C. Ballif, *J. Phys. Chem. Lett.* **2014**, *5*, 1035.
[5] H. Tan, A. Jain, O. Voznyy, X. Lan, F. P. García de Arquer, J. Z. Fan, R. Quintero-Bermudez, M. Yuan, B. Zhang, Y. Zhao, F. Fan, P. Li, L. N. Quan, Y. Zhao, Z.-H. Lu, Z. Yang, S. Hoogland, E. H. Sargent, *Science* **2017**, *355*, 722.
[6] M. Kim, G.-H. Kim, T. K. Lee, I. W. Choi, H. W. Choi, Y. Jo, Y. J. Yoon, J. W. Kim, J. Lee, D. Huh, H. Lee, S. K. Kwak, J. Y. Kim, D. S. Kim, *Joule* **2019**, *3*, 2179.
[7] X. Yang, Y. Ni, Y. Zhang, Y. Wang, W. Yang, D. Luo, Y. Tu, Q. Gong, H. Yu, R. Zhu, *ACS Energy Lett.* **2021**, *6*, 2404.
[8] L. K. Ono, S. Liu, Y. Qi, *Angew. Chem., Int. Ed.* **2020**, *59*, 6676.
[9] J. Chen, N.-G. Park, *Adv. Mater.* **2019**, *31*, 1803019.
[10] M. M. Lee, J. Teuscher, T. Miyasaka, T. N. Murakami, H. J. Snaith, *Science* **2012**, *338*, 643.
[11] K. Wang, W. S. Subhani, Y. Wang, X. Zuo, H. Wang, L. Duan, S. Liu, *Adv. Mater.* **2019**, *31*, 1902037.
[12] T. Li, Y. Pan, Z. Wang, Y. Xia, Y. Chen, W. Huang, *J. Mater. Chem. A* **2017**, *5*, 12602.
[13] F. Zhang, K. Zhu, *Adv. Energy Mater.* **2020**, *10*, 1902579.
[14] W. Chi, S. K. Banerjee, *Chem. Eng. J.* **2021**, *426*, 131588.
[15] W. Chi, S. K. Banerjee, *Adv. Funct. Mater.* **2022**, *32*, 2200029.
[16] L. Hu, L. Duan, Y. Yao, W. Chen, Z. Zhou, C. Cazorla, C. H. Lin, X. Guan, X. Geng, F. Wang, T. Wan, S. Wu, S. Cheong, R. D. Tilley, S. Liu, J. Yuan, D. Chu, T. Wu, S. Huang, *Adv. Sci.* **2022**, *9*, 2102258.
[17] S. S. Mali, J. V. Patil, S. R. Rondiya, N. Y. Dzade, J. A. Steele, M. K. Nazeeruddin, P. S. Patil, C. K. Hong, *Adv. Mater.* **2022**, *34*, 2203204.
[18] Z. Luo, W. Yin, J. Wang, Y. Hua, Z. Zhou, W. Zhang, S. Chen, X. Zhang, W. Zheng, *Adv. Funct. Mater.* **2025**, *35*, 2419268.
[19] J. Lin, L. Wang, X. Meng, W. Li, N. Ren, L. Tao, J. Xiao, Q. Jing, Y. Song, H. Zhao, *Appl. Phys. Lett.* **2025**, *126*, 043904.
[20] W. Xiang, X. Gu, K. Khawaja, M. Yuan, C. Picart, L. Li, F. Yan, *Carbon* **2025**, *235*, 120034.
[21] X. Zheng, J. Troughton, N. Gasparini, Y. Lin, M. Wei, Y. Hou, J. Liu, K. Song, Z. Chen, C. Yang, B. Turedi, A. Y. Alsalloum, J. Pan, J. Chen, A. A. Zhumekenov, T. D. Anthopoulos, Y. Han, D. Baran, O. F. Mohammed, E. H. Sargent, O. M. Bakr, *Joule* **2019**, *3*, 1963.
[22] Q. Yu, W. Sun, S. Tang, *Nanomaterials* **2024**, *14*, 1651.
[23] P. Tipparak, W. Passatorntaschakorn, W. Khampa, W. Musikpan, C. E. Usulor, C. Bhoomanee, S. Singh, A. Gardchareon, A. Ngamjarurojana, P. Ruankham, D. Wongratanaphisan, *ACS Appl. Energy Mater.* **2025**, *8*, 355.
[24] C. Liu, X. Zhen, W. Peng, K. Huang, L. Zhang, Z. Li, X. Zhou, J. Chen, L. Chu, W. Yan, K. Fukuda, Y. Sheng, X. Wang, C. Liu, *Adv. Energy Mater.* **2025**, *15*, 2405074.
[25] J. Ni, J. Guan, M. Hu, R. Wang, Z. Yang, J. Li, S. Zhang, S. Li, J. Li, H. Cai, J. Zhang, *ACS Appl. Energy Mater.* **2023**, *6*, 11090.
[26] T. T. Ngo, S. Masi, P. F. Mendez, M. Kazes, D. Oron, I. M. Seró, *Nanoscale Adv.* **2019**, *1*, 4109.
[27] J. Han, X. Yin, H. Nan, Y. Zhou, Z. Yao, J. Li, D. Oron, H. Lin, *Small* **2017**, *13*, 1700953.
[28] L. Givalou, E. Christopoulos, M. K. Arfanis, S. Orfanoudakis, P. Tsipas, A. Dimoulas, T. Stergiopoulos, P. Falaras, *Electrochim. Acta* **2024**, *473*, 143523.
[29] Q. Cai, W. Sheng, J. Yang, Y. Zhong, S. Xiao, J. He, L. Tan, Y. Chen, *Adv. Funct. Mater.* **2023**, *33*, 2304503.
[30] M. Wang, L. Gao, P. Yu, Q. Wang, C. Yu, X. Zhang, Y. Wang, W. Zheng, J. Zhang, *J. Mater. Chem. C* **2022**, *10*, 5134.
[31] S. Aftab, F. Kabir, M. Mukhtar, I. Hussain, G. Nazir, M. Aslam, H. H. Hegazy, M. A. Yewale, *Nano Energy* **2024**, *129*, 109995.
[32] C. Li, D. Yao, P. Dong, Z. Tang, Y. Li, B. Chen, N. Tian, G. Zheng, Y. Peng, F. Long, *Appl. Surf. Sci.* **2024**, *658*, 159848.
[33] B. Alessi, A. U. Kambley, C. McDonald, Z. Xu, T. Matsui, V. Svrcek, *Nano Energy* **2024**, *128*, 109846.
[34] X. Li, S. Aftab, S. Hussain, F. Kabir, A. M. A. Henaish, A. G. Al-Sehemi, M. R. Pallavolu, G. Koyyada, *J. Mater. Chem. A* **2024**, *12*, 4421.
[35] X. Li, S. Aftab, M. Mukhtar, F. Kabir, M. F. Khan, H. H. Hegazy, E. Akman, *Nanomicro Lett.* **2024**, *17*, 28.
[36] W. Qin, R. A. Shah, P. Guyot-Sionnest, *ACS Nano* **2012**, *6*, 912.
[37] H.-J. Zhan, P.-J. Zhou, Z.-Y. He, Y. Tian, *Eur. J. Inorg. Chem.* **2012**, *2012*, 2487.
[38] M. Green, *J. Mater. Chem.* **2010**, *20*, 5797.
[39] M. Boles, D. Ling, T. Hyeon, D. Talapin, *Nat. Mater.* **2016**, *15*, 141.
[40] F. G. Ortiz Calderon, B. S. Gómez Pineros, N. D. McClenaghan, G. Granados-Oliveros, *J. Fluoresc.* **2025**, *35*, 4385.

[41] S. Lim, D. H. Lee, H. Choi, Y. Choi, D. G. Lee, S. B. Cho, S. Ko, J. Choi, Y. Kim, T. Park, *Nano-Micro Lett.* **2022**, *14*, 204.
[42] M. Qin, P. F. Chan, X. Lu, *Adv. Mater.* **2021**, *33*, 2105290.
[43] Z. Chen, F. Wu, R. Pathak, L. Chen, J. Bian, S. Mabrouk, J. Elam, Q. Qiao, *Adv. Electron. Mater.* **2024**, *10*, 2400107.
[44] C. Hanmandlu, S. Swamy, A. Singh, C. Hsin-An, C.-C. Liu, C.-S. Lai, A. Mohapatra, C.-W. Pao, P. Chen, C.-W. Chu, *J. Mater. Chem. A* **2020**, *8*, 5263.
[45] T. N. Ly, S. Park, *Sci. Rep.* **2018**, *8*, 18030.
[46] G. Kresse, J. Furthmüller, *Phys. Rev. B* **1996**, *54*, 11169.
[47] G. Kresse, D. Joubert, *Phys. Rev. B* **1999**, *59*, 1758.
[48] P. E. Blöchl, *Phys. Rev. B* **1994**, *50*, 17953.
[49] J. Perdew, K. Burke, M. Ernzerhof, *Phys. Rev. Lett.* **1996**, *77*, 3865.
[50] M. Burgelman, P. Nollet, S. Degrave, *Thin Solid Films* **2000**, *361*, 527.